

Influence of Shape Resonances on the Angular Dependence of Molecular Photoionization Delays

F. Holzmeier^{1,2,*†}, J. Joseph¹, J. C. Houver¹, M. Lebech³, D. Doweck¹, R. R. Lucchese^{4,†}

¹Université Paris-Saclay, CNRS, Institut des Sciences Moléculaires d'Orsay, 91405, Orsay, France.

²Université Paris-Saclay, Synchrotron SOLEIL, 91190, Saint Aubin, France.

³Niels Bohr Institute, University of Copenhagen, Copenhagen, Denmark.

⁴Lawrence Berkeley National Laboratory, Berkeley, California, 94720, USA.

*Correspondence to: fabian.holzmeier@imec.be, rlucchese@lbl.gov

†Present address: imec, 3001, Leuven, Belgium.

Characterizing time delays in molecular photoionization as a function of the ejected electron emission direction relative to the orientation of the molecule and the light polarization axis provides unprecedented insights into the attosecond dynamics induced by extreme ultraviolet or X-ray one-photon absorption, including the role of electronic correlation and continuum resonant states. Here, we report completely resolved experimental and computational angular dependence of single-photon ionization delays in NO molecules across a shape resonance, relying on synchrotron radiation and time independent ab initio calculations. The angle-dependent time delay variations of few hundreds of attoseconds, resulting from the interference of the resonant and non-resonant contributions to the dynamics of the ejected electron, are well described using a multichannel Fano model where the resonance time delay is angle-independent. Comparing these results with the same resonance computed in e-NO⁺ scattering highlights the connection of photoionization delays with Wigner scattering time delays.

The interaction of a single XUV photon with a molecule induces ultrafast photoionization dynamics, in which electronic coherences and many-body interactions, including couplings between electron and nuclear motions, are pivotal^{1,2}. In addition, resonances, i.e., quasi-bound states in the ionization continuum, often have a significant impact on the dynamics due to enhanced cross sections or trapping of the outgoing electron. Characterizing the photoionization dynamics in molecules at its natural timescale stands therefore as a vital research field at the forefront of attosecond science^{3,4}.

In recent years photoionization time delays were characterized in real-time pioneering experiments where one-photon ionization induced by an XUV attosecond pulse is probed in a delayed femtosecond IR field using RABBITT⁵ or streaking⁶ techniques. For atomic targets, one-photon ionization delays could be retrieved from the time-dependence of the oscillatory two-photon ionization signal demonstrating, e.g., relative photoionization time delays of few tens of attoseconds between electron ejection from ns and np electronic orbitals in Ne and Ar^{7,8} or addressing the characterization of autoionizing Fano resonances in the ionization continuum⁹⁻¹¹. More insight into such ionization dynamics described by two-photon transition matrix elements was then demonstrated in angular resolved studies in the laboratory frame¹²⁻¹⁸.

Measuring photoionization delays in molecular targets using similar techniques is more challenging. First, the higher density of electronic states and their intrinsic energy width result in congested electron energy spectra when ionization is induced by the broadband XUV pulse and probed by the IR fundamental field. Using RABBITT attosecond interferometry where the

XUV spectrum consists of a harmonic frequency comb allowing for spectral resolution, this could be circumvented to some extent, providing photoionization delays between different valence ionic states of randomly oriented small molecular targets¹⁹⁻²³. It was proven e.g. that shape resonances, caused by the transient trapping of the photoelectron in an angular momentum barrier²⁴ structuring the continuum of ionic states, can lead to positive two-photon ionization delays larger than one hundred attoseconds²⁰⁻²³. Meanwhile, it was recognized that the latter observables do not give access to the one-photon ionization dynamics, due to the complexity inherent to the non-spherical symmetry of the molecular objects^{20,25}. Addressing the angular dependence of the photoionization dynamics in molecules as well adds complexity since, even for the simplest diatomic molecules, it depends on both the orientation of the molecule relative to the light quantization axis $\hat{\Omega}$, and the emission direction of the photoelectron in the molecular frame (MF) $\hat{k} \equiv (\theta_k, \phi_k)$.

The one-photon ionization time delay $\tau(\hat{k}, \hat{\Omega}, E)$, where E is the electron energy, is defined as the energy derivative of the phase $\eta(\hat{k}, \hat{\Omega}, E)$ of the complex-valued angle-dependent photoionization dipole amplitude (PDA) $D(\hat{k}, \hat{\Omega}, E)$,

$$\tau(\hat{k}, \hat{\Omega}, E) = \frac{d\eta(\hat{k}, \hat{\Omega}, E)}{dE} \quad (1)$$

which is equivalent to the definition of the group delay for a wavepacket. Energy and MF angle-resolved attosecond photoionization delays for specific orientations of a diatomic molecule parallel or perpendicular relative to the axis of linearly

polarized light were theoretically predicted for single-photon valence ionization of, e.g., N_2 and CO ²⁶, highlighting indeed a strong anisotropy of the ionization dynamics. The rich angular patterns were attributed to the intrinsic anisotropy of the molecular potential featuring the electronic structure of the ionized molecular states and accounted for by the interference of the many partial waves with quantum numbers (l, m) building up the electron wave packet in the continuum.

Initial experimental evidence of an orientation-dependent anisotropy of the dynamics was demonstrated in RABBITT studies addressing non-resonant inner valence ionization of CO through the determination of stereo Wigner time delays, i.e., the difference in time delay for emission within a 2π solid angle towards the C and O ends of the molecule²⁷, or dissociative ionization of H_2 in presence of autoionizing resonances and coupling between electron and nuclear motions²⁸.

In the present study, experimental and computed photoionization time delays with complete angular resolution in the molecular frame (MF) are reported and analyzed in terms of the influence of a well identified σ^* shape resonance²⁹ in inner-valence ionization of the NO molecule. Experimental ionization delays are obtained from single-photon ionization measurements of molecular frame photoelectron angular distributions

(MFPADs)^{30,31} using synchrotron radiation at a series of well-resolved photon energies. In order to interpret the observed energy and MF angle-resolved dynamics, varying within a few hundreds of attoseconds, a multichannel Fano formalism is presented, from which we obtain separately the contributions of resonant and non-resonant photoionization amplitudes that coherently add to yield the total PDA. The results demonstrate that the angular dependence of the MF-resolved time delays is a signature of the interference between the resonant and non-resonant components of the PDA, where the ionization delay of the resonant component is angle-independent. Beyond the increase by π of the scattering phase shift across a resonance³², we show that in resonant molecular photoionization the PDA phases for different emission directions can change by values ranging from 0 to 2π , giving rise to diverse angle-dependent time delay energy profiles. These behaviors can be most conveniently predicted by considering the curve formed by the PDA in the complex plane when plotted at different energies, for selected emission angles in the molecular frame. Finally, a comparison with the same resonance computed in $e-NO^+$ scattering gives more insight into the connection between Wigner scattering time delays and photoionization time delays.

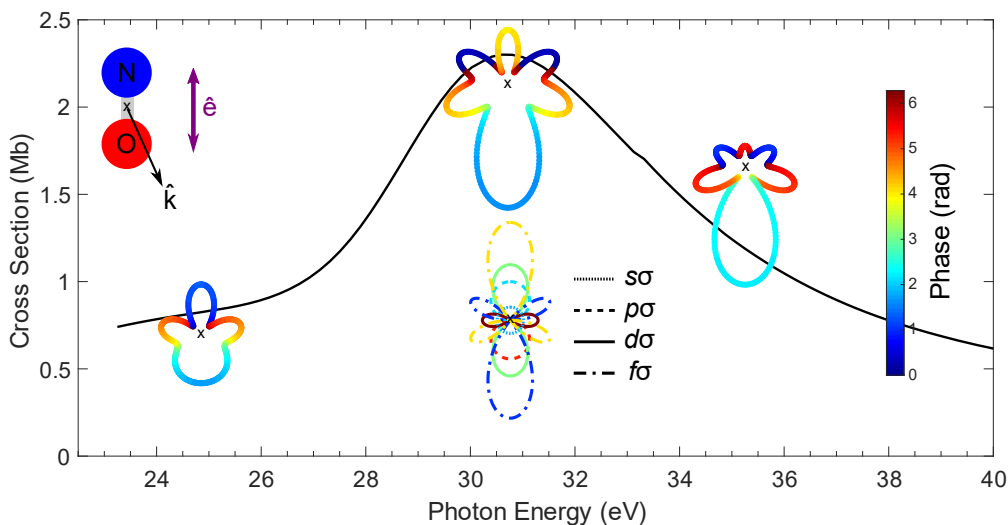


Fig. 1 Resolving the complex valued photoionization amplitudes in the molecular frame across a shape resonance. Energy dependence of the complex-valued photoionization dipole amplitudes for the ionization of NO leading to the $(4\sigma)^{-1} c^3\Pi$ state of NO^+ plotted as a function of the emission direction \hat{k} in the molecular frame for molecules oriented parallel to linearly polarized light in the region of the NO $4\sigma \rightarrow k\sigma$ shape resonance. The computed magnitudes and phases are represented by the radius vector and the color of the line plots, respectively. The energy derivative of the PDA phases gives access to photoionization time delays. For a photon energy of 31 eV at the peak of the resonance, the PDAs are dominated by the coherent superposition of partial waves up to $l=3$ as shown.

Results

Angle-resolved photoionization time delays across the NO shape resonance

MF angle-resolved photoionization delays for single-photon ionization of the NO molecule into the $NO^+(c^3\Pi)$ inner valence ionic state are extracted from the MFPADs measured using circularly polarized synchrotron radiation³³, for a series of eleven well resolved photon energies probing the 23.25-38.75 eV

range at equal steps of 1.55 eV (see Methods). This region covers the well identified $4\sigma \rightarrow k\sigma^*$ shape resonance assigned to ionization into the $NO^+(c^3\Pi)$ for the parallel transition, featured by a light polarization parallel to the molecular axis³⁴, with a maximum of the cross section occurring around 31 eV photon energy (~ 9 eV photoelectron energy). The MFPAD, i.e., the photoemission probability along $\hat{k} \equiv (\theta_k, \phi_k)$ in the molecular frame for any orientation of the molecule $\hat{\Omega}$ relative to the light quantization axis, is proportional to the absolute square of the

complex valued photoionization dipole amplitude $D(\hat{k}, \hat{\Omega}, E)$. The latter is written as a coherent superposition of the partial wave dipole matrix elements (DMEs) $D_{l,m,\mu}$ with an angular dependence described by the spherical harmonic $Y_{l,m}(\hat{k})$, as:

$$D(\hat{k}, \hat{\Omega}, E) = \sum_{\mu} \sum_{l,m} D_{l,m,\mu}(E) Y_{l,m}(\hat{k}) R_{\mu,h}^{(1)}(\hat{\Omega}), \quad (2)$$

where $R_{\mu,h}^{(1)}(\hat{\Omega})$ is the matrix rotating the molecule into the field frame defined by the Euler angles $\hat{\Omega} \equiv (\gamma, \chi, \beta)$, and μ is the projected angular momentum of the photon on the MF axis, with h indicating the light polarization (see Supplementary Note 3). The partial wave expansion of the photoionization dipole amplitude in Eq. (2) is at the core of the derivation of the ionization delays defined in Eq. (1). This approach is sketched in Fig.1 for an orientation of the molecule parallel to the polarization axis.

In the experiment, the first major step consists of extracting the complex valued $D_{l,m,\mu}$ DMEs for the individual (l, m) partial-waves from the measured MFPADs, their magnitudes d_{lm} and relative phases $\tilde{\eta}_{lm}$, for each measured photon/electron energy^{35,33} across the shape resonance. A finer sampling of the region of the resonance is achieved using a spline fit of the measured $D_{l,m,\mu}$ magnitudes and relative phases (see Supplementary Note 4). Eq. (2) then provides the corresponding PDAs for any MF emission direction \hat{k} and orientation of the molecule $\hat{\Omega}$, their magnitude and phase $\eta(\hat{k}, \hat{\Omega}, E)$. In order to establish a coherence between the phases of the PDAs for different energies, the relative phases of the partial wave DMEs extracted for each energy were based on a common reference: in the presence of a resonance, it is advantageous to choose a reference DME $D_{l,m,\mu}$ that is not coupled to the resonance (see Supplementary Notes 4 & 5). Finally, photoionization time delays are obtained as the energy derivative of the PDA phases according to Eq. (1).

In the following we focus on the PDAs with NO oriented parallel to the axis of linearly polarized light, which highlights the interference between the shape resonance and the non-resonant direct ionization channel in the parallel transition. Each PDA is thus characterized by the single polar angle θ_k due to the cylindrical symmetry of MF photoemission in that case, and it involves solely $(l, 0) \equiv (l, \sigma)$ partial waves, with here $l_{\max} = 3$. Experimental data are compared with time-independent calculations using the multi-channel Schwinger configuration interaction method (see Methods) providing computed DMEs and PDAs relying on Eq. (2).

Fig. 2 shows, for both experiment and theory, two-dimensional (2D) maps representing the magnitudes and phases of the PDAs for the parallel orientation resulting from the coherent superposition of the $(l, 0)$ partial-wave DMEs according to Eq. (2), together with the 2D map of the photoionization time delays obtained as the energy derivatives of the PDA phases following Eq. (1), as a function of the photoelectron energy E and the emission direction θ_k . The reported PDA phases are obtained by referencing the D_{lm} dipole matrix element phases to the $\eta_{2,1}$ phase as described above.

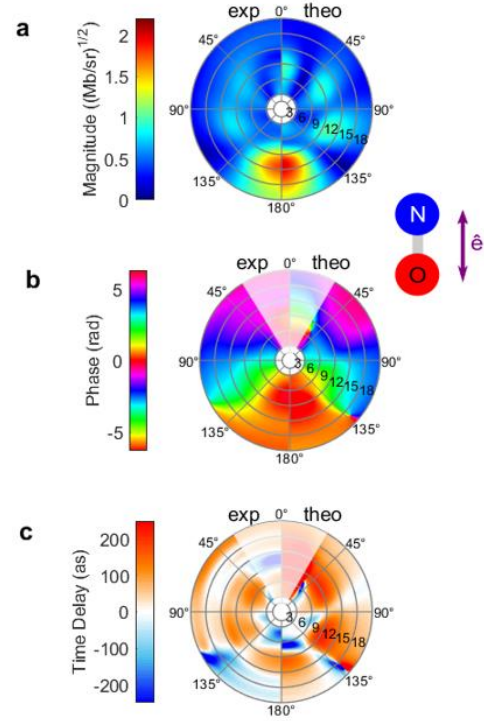


Fig. 2 Magnitude and phase of PDAs and photoionization time delays. Polar plots of **a** the PDA magnitudes, **b** PDA phases and **c** photoionization time delays. The left (right) half of each map corresponds to the experimental (computed) data. The radial distance from the center of the maps gives the photoelectron kinetic energy E in eV. The polar angle θ_k is relative to the NO molecular axis, with $(\theta_k = 0^\circ)$ corresponding to the direction of the N atom. In this and all subsequent figures, magnitudes have been multiplied by $\sqrt{4\pi^2 h\nu/c}$ so that their absolute squares yield the differential cross section in Mbarn/steradian. See text and Fig. S4 (Supplementary Note 7) for corresponding uncertainties.

The common features of the measured and computed PDAs are highlighted by comparing the left and right halves of each of the 2D maps. Phases and time delays for an emission cone of 0 - 30° are attenuated in this visualization, since the emission probability in direction of the N atom is quite weak as visible in Fig. 2a and ref.²⁹ and phases are therefore less well-defined. Complementary one-dimensional plots featuring the energy dependence of the PDA magnitudes, phases, and time delays for a series of selected fixed emission angles between 45° and 180° , are reported in Fig.S4 (Supplementary Note 7), including uncertainties for the experimental results.

Experiment and theory demonstrate very similar features in the polar plot of the magnitudes of the PDAs, consistent with those observed in the MFPADs²⁹. A distinct up-down asymmetry, characterized by a strongly favored emission probability towards the oxygen end of the NO molecule ($\theta_k = 180^\circ$) at energies higher than 8 eV ($h\nu \geq 30$ eV), is observed within the structured pattern with four lobes reflecting the important contribution of the $f\sigma$ partial wave, which display a maximum in the 9 - 12 eV electron energy range.

The structure observed in the PDA magnitudes is also evident in the map showing the PDA phases in Fig. 2b and the photoionization time delays in Fig. 2c, demonstrating a significant MF anisotropy of the emission dynamics as well (see Fig.S4). The measured PDA phases, with specific mean values for the different angle sectors, display slope variations about the resonance, while the global phase change before or after the resonance ranges between 0 and π . For the lobes of maximum photoionization probability, around $\theta_k = 180^\circ, 120^\circ$ or 60° , the measured time delay reaches +100 as on top of the resonance, while it is near zero or slightly negative in between. A remarkable structured energy profile is observed for the $\theta_k = 150\text{-}180^\circ$ preferred emission cone, where the time delay passes through a minimum of -215 as at about 3-5 eV electron energy before rising up to +110 as at 9 eV, then flattening out to zero for higher energies. This overall behavior agrees qualitatively very well with the computed time delay energy profiles, although in the calculation the extreme values in this emission cone vary from -400 as to +160 as. A better quantitative agreement can be expected from calculations beyond the fixed nuclei approximation²³. Large positive and negative group delays in the region of shape and autoionization resonances have also been observed in high-harmonic spectroscopy involving aligned N_2 molecules³⁶. Localized discontinuities are observed, e.g., at ($\theta_k = 135^\circ$; $E=12\text{-}18$ eV) when the PDA goes through zero³⁵, together with a phase jump, similar to a Cooper minimum. Relying on the presented extraction of the complex-valued DMEs from measured MFPADs³⁷ in photoionization of small molecules, single-photon ionization delays, thereby reported with a complete angular and energy resolution for an orientation parallel to the polarization axis, are as well accessible for any orientation of the molecule and MF emission direction $\hat{k} \equiv (\theta_k, \phi_k)$.

Behavior of MF angle-resolved PDA Curves in a shape Resonance.

The ionization delay energy profiles across the resonance for fixed MF emission directions θ_k can be rationalized by considering the energy dependence of the $D(\theta_k, E)$ PDAs as curves in the complex plane, resulting from the evolution of their real and imaginary parts with electron energy. This representation previously used to visualize the behavior of DMEs near Cooper minima³⁵, or the spectral phase profile of autoionizing resonances¹⁰, is here exploited to feature the influence of the shape resonance onto the energy dependence of MF angle resolved channels. In Fig. 3 we present the PDA curves and the corresponding time delays for the experiment and calculations, at emission angles of 180° and 60° .

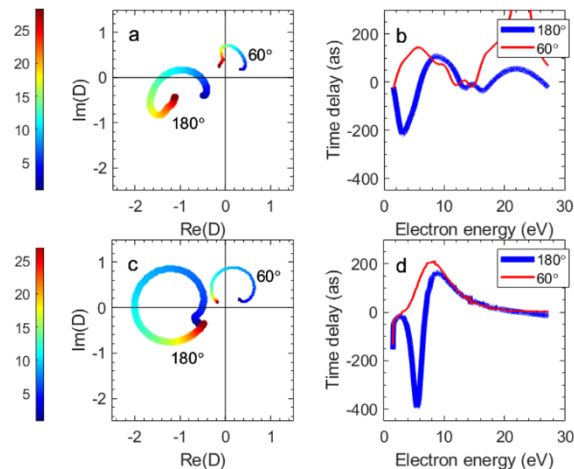


Fig. 3 Experimental and computed PDA curves and time delays. **a** PDA curves and **b** time delays for the experiment at emission angles of 180° (thick line, blue in b) and 60° (thin line, red in b). The corresponding data for the computed cross sections are given in **c** and **d**. The color scale on the left gives the photoelectron energy in eV for the curves in the complex plane.

The evolution of the PDA in the complex plane with increasing energy is fairly similar in the experimental and computed data. The PDA at 180° describes nearly a full circle centered away from the origin in the third quadrant of the complex plane, yielding a very small overall phase change and therefore both large positive and negative time delays. For 60° , the PDA is shifted away from the origin in the first quadrant leading to an overall phase change smaller than π , and mostly positive time delays. A qualitative understanding of these different types of curves relying on a multichannel model of the behavior of the PDA across a resonance is discussed in the following section, and further illustrated in Supplementary Note 8.

Partial Wave Multichannel Fano Line-Shape Analysis of a shape Resonance

The remarkable photoionization dynamics featured in Fig. 2 in the region of the $4\sigma \rightarrow k\sigma^*$ shape resonance can be interpreted based on a Fano line-shape analysis³⁸ as applied to multichannel problems³⁹⁻⁴¹. The analysis models the contributions of resonant and non-resonant photoionization amplitudes that coherently add to yield the total PDA. The rich angular variation of the time delay is found to stem from the interference of the resonant and non-resonant paths, where the resonance time delay is angle-independent.

In the original Fano analysis of photoionization with a resonance coupled to a continuum³⁸, the resulting line shapes were characterized by a position, E_{res} , width, Γ , and line-shape parameter, q . For a single resonance coupled to more than one asymptotic continuum, it was shown that the analysis could be transformed to that of the resonant state decaying to a single channel plus a sum of non-interacting channels formed as linear combinations of the original channels. Later developments³⁹⁻⁴¹ provided expressions for the line shapes for decay to the original asymptotic channels, which when added together yield the same profiles as found in the original paper by Fano. Two-channel Fano-like parameterizations have recently been applied to

predict the angular dependence of atomic photoionization time delays in the laboratory frame¹⁴.

In the present study, implementing a multichannel analysis based on the expansion of the PDA as a coherent superposition of partial-wave channels (Eq. (2)), we show that the experimental and computed PDAs are very well fitted using a set of partial wave independent E_{res} , and q Fano parameters, and a total width Γ , defining a single resonant state.

For ionization from the 4σ orbital by light linearly polarized parallel to the molecular axis, with $m = 0$, $\mu = 0$, and $R_{0,0}^{(1)}(\hat{\Omega} = \hat{z}) = 1$, the PDA in Eq. (2) writes as:

$$\begin{aligned} D(\theta_k, \varepsilon) &= \sum_l D_l(\varepsilon) Y_{l0}(\hat{k}) \\ &= \sum_l D_l(\varepsilon) \sqrt{\frac{2l+1}{4\pi}} P_l(\cos \theta_k). \end{aligned} \quad (3)$$

where ε is the energy relative to the resonance energy E_{res} , scaled by the resonance width Γ

$$\varepsilon = \frac{E - E_{\text{res}}}{\Gamma/2}. \quad (4)$$

For such a resonant state decaying into multiple partial waves, the $D_l(\varepsilon)$ DMEs can be expressed as the sum⁴¹

$$D_l(\varepsilon) = D_l^{(0)}(\varepsilon) + D_l^{\text{res}}(\varepsilon) \quad \text{for } l = 0, \dots, l_x \quad (5)$$

where $D_l^{(0)}(\varepsilon)$ and $D_l^{\text{res}}(\varepsilon)$ are non-resonant and resonant contributions for each partial wave. The $D^{(0)}(\theta_k, \varepsilon)$ non-resonant and $D^{\text{res}}(\theta_k, \varepsilon)$ resonant contributions to the $D(\theta_k, \varepsilon)$ PDA in Eq. (3) are then given by:

$$D^{(0)}(\theta_k, \varepsilon) = \sum_l D_l^{(0)}(\varepsilon) \sqrt{\frac{2l+1}{4\pi}} P_l(\cos \theta_k) \quad (6)$$

and (see Methods for details)

$$\begin{aligned} &D^{\text{res}}(\theta_k, \varepsilon) \\ &= \frac{q-i}{\varepsilon+i} \sum_l \alpha_l(\varepsilon) \sqrt{\frac{2l+1}{4\pi}} P_l(\cos \theta_k) \end{aligned} \quad (7)$$

Performing a non-linear least squares fit of the PDAs, either computed or obtained from the experiment, based on the above general form of $D^{(0)}(\theta_k, \varepsilon)$ and $D^{\text{res}}(\theta_k, \varepsilon)$, enables us to determine the resonance energy, E_{res} , the Fano line-shape parameter q , as well as the complex valued $D_{l,n}^{(0)}$, i.e., the non-resonant DMEs, and the V_l couplings between the resonant state and each partial wave directly related to the partial widths Γ_l (see Eq. (4) and Methods).

Table 1 Root-mean-square (RMS) deviation and fitting parameters of the Fano fit. Results obtained in the non-linear least square fit of the experimental and computed PDA with the multichannel Fano model (see text and Methods).

	<i>experiment</i>	<i>computation</i>
<i>RMS fit</i>	0.014	0.011
E_{res} (eV)	8.29	8.24
q	2.709	1.690
Γ (eV)	7.958	6.640
Γ_0 (eV)	0.014	0.043
Γ_1 (eV)	0.031	0.267
Γ_2 (eV)	1.121	0.114
Γ_3 (eV)	6.791	6.163
Γ_4 (eV)	--	0.053

The obtained fitting parameters are summarized in Table 1 and the subsequent separate resonant and non-resonant components of the transition are presented in Fig. 4 in terms of the magnitudes (a,b) and phases (c,d) of the PDAs, and the energy derivatives of the phases expressed as time delays (e,f), for both experiment (left half) and theory (right half). In the plot of the PDA magnitude for the resonant component (Fig. 4a), both show the dominant f -wave nature of the resonance, with large partial widths of the order of 6.5 eV for $l = 3$. For the non-resonant component of the transition, the measured and computed PDA magnitudes (Fig. 4b) display an asymmetry along the molecular axis favoring emission at ($\theta_k = 180^\circ$), reflecting the interference of $l\sigma$ partial waves of different parity. The phases (c,d), e.g. roughly out-of-phase and in-phase for the 0° - 30° and 150° - 180° emission cones, respectively, determine the coherent superposition of the resonant and non-resonant components of the PDA, with magnitudes described in (a,b), resulting in the PDA displayed in Fig. 2.

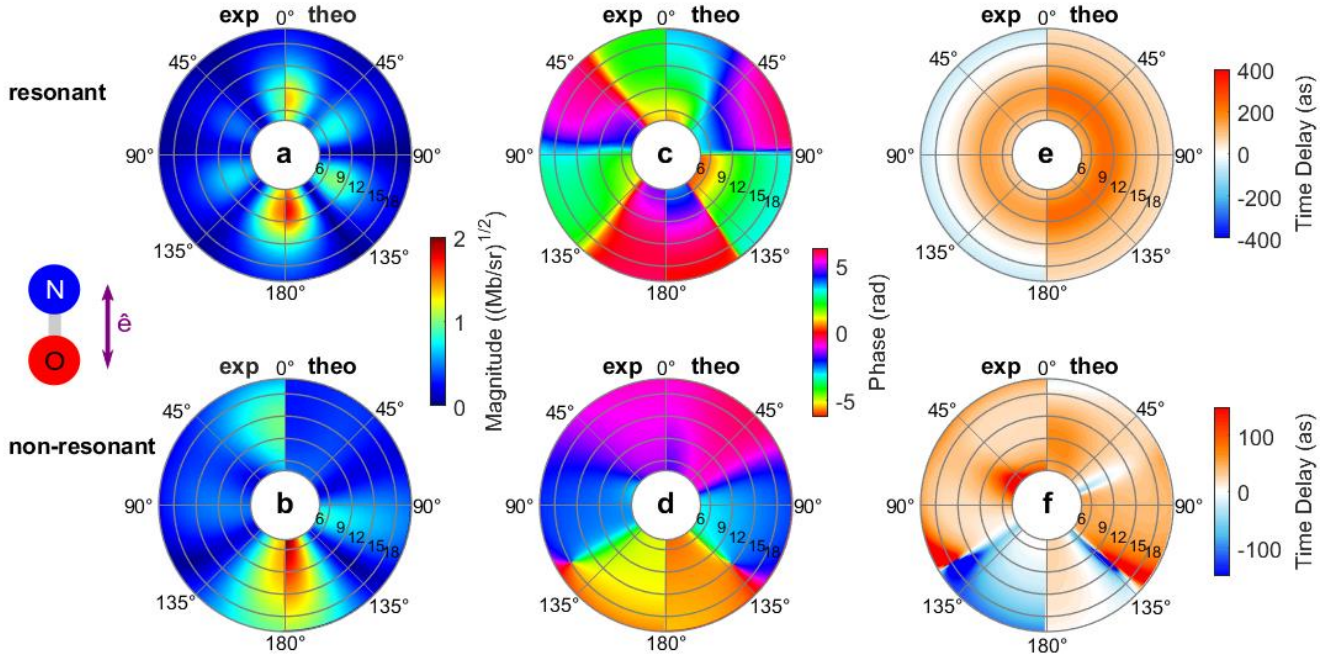


Fig. 4 Resonant and non-resonant PDAs and photoionization delays. Resonant (top) and non-resonant (bottom) PDA magnitudes (a, b), phases (c, d) and energy derivative of the phases representing the time delays (e, f). The respective left (right) halves of the 2D maps show the data extracted from the experiment (theory). In the 2D polar plots, the radius indicates the photoelectron kinetic energy in eV, and the polar angle θ_k is relative to the molecular axis, with ($\theta_k = 0^\circ$) pointing to the direction of the N atom. Note that the non-resonant time delays are on a reduced scale compared to the resonant ones. For both the computed and experimental data, we obtain a very good fit of the PDAs for θ_k between 0° and 180° , at electron kinetic energies from 4.65 eV to 17.05 eV: this energy range includes the shape resonance in the $c^3\Pi$ channel but excludes resonant contributions from other channels which strongly affect the PDAs below 4.65 eV. This supports the validity of the proposed multi-channel Fano model.

The nodal structures seen in the magnitudes in Fig. 4a and Fig. 4b lead to discontinuous jumps of π in the phases depicted in Fig. 4c and Fig. 4d as the emission angle direction crosses such an angular node. When the emission angle location of a node has some energy dependence, i.e., in the radial direction as seen in Fig. 2b and Fig. 4d around 135° , then rapid phase changes by π occur as a function of energy leading to the large positive and negative photoionization time delays in Fig. 2c and Fig. 4f. The plot of the ionization delays for the resonant component (Fig. 4e) displays a positive maximum on top of the resonance of the order of 150 as for the experiment, and 250 as for the calculation, consistent with the trapping effect resulting from the centrifugal barrier associated with the shape resonance. We stress that they display no angular dependence: this characteristic linked to the multichannel Fano model presented (see Methods) is validated by the excellent fit of the model to the reported results (Table 1). It is a reflection of the general observation in photoionization or electron scattering that for resonances narrower than changes in any non-resonant scattering in the vicinity of the resonance, one will measure a single lifetime, but possibly different amplitudes, for the different decay channels. We also note that in Fig. 4e the computed resonant time delay is always positive, whereas the experimental time delay, dominantly positive, reaches negative values for high energies. This feature can be assigned to the different energy dependence of the non-resonant $D_i^0(\epsilon)$ included in the model fits. On the

other hand, the corresponding non-resonant ionization delays display emission anisotropies assigned to the combination of the non-resonant scattering and the dipole coupling of the initial state to the continuum which can be analyzed in terms of the partial-wave composition of the 4σ orbital from which the photoelectron is ejected⁴². Some features common to the experimental and computed PDAs are visible, e.g., in the discontinuities corresponding to the PDA nodal structures around 135° in theory and 120° in the experiment (Fig. 4f), reflecting those observed in Fig. 2c. Consequently, within the multichannel Fano model, all the polar angle dependence in the time delay energy profiles reported in Fig. 2c for the full PDA originates from the interference between the resonant and non-resonant components of the PDA, where the ionization delay of the resonant term is angle-independent.

Relationship Between Wigner Scattering Time Delay and Photoionization Time Delay

The analysis of the MF angle-resolved time delays in the presence of a shape resonance within the presented multichannel Fano model motivates a closer comparison of the resonant photoionization time delay, which displays no angular dependence in the MF, with a computed Wigner scattering time delay in the presence of a resonance. We find that the resonant part of the photoionization time delay is comparable to half of the resonant Wigner scattering time delay.

First introduced in scattering theory, the so-called Eisenbud-Wigner-Smith time delay, or Wigner scattering time delay, defined as the delay of a wave packet scattering from a target relative to that of a free wave packet, is given by twice the energy derivative of the scattering phase shift^{43,44}.

For the resonant part of the PDA in the multichannel Fano fit, D^{res} , as defined in Eq. (7), the energy derivative of the phase leads to the photoionization time delay

$$\tau_{\text{res}} = \frac{2}{\Gamma} \frac{d\eta_{\text{PDA}}}{d\varepsilon} = \frac{2}{\Gamma} \frac{1}{1 + \varepsilon^2} \quad (8)$$

where the relative energy ε is defined in Eq. (4) and we have assumed that there is no energy dependence in the phase of $\alpha(\varepsilon)$. Note that this is the same time delay as would be obtained from D^{res} in the limit of the $D_l^0 \rightarrow 0$ (see Methods). This expression matches that corresponding to the energy derivative of the scattering phase shift, δ_{Scat} , for a resonance fit by the Breit-Wigner form⁴⁵, or its multichannel generalization³², which is

$$\frac{1}{2} \tau_{W-\text{res}} = \frac{2}{\Gamma} \frac{d\delta_{\text{Scat}}}{d\varepsilon} = \frac{2}{\Gamma} \frac{1}{1 + \varepsilon^2} \quad (9)$$

where $\tau_{W-\text{res}}$ is the resonant Wigner scattering time delay.

To illustrate this close correspondence between the resonant parts of the scattering Wigner time delay and the photoionization time delay for the studied reaction, we have computed the eigenphase sums³² from the short-range scattering matrix for electron scattering from the NO^+ ion using similar computational methods as were used for the photoionization calculation (see Supplementary Note 5).

The fit of the computed eigenphase sum displayed in Fig. 5a using the Breit-Wigner form³² leads to the resonance position, 9.09 eV, and width, 6.07 eV. When scattering also involves a non-resonant background component, as seen in the negative slope of the eigenphase sum before and after the resonance in Fig. 5a, the phase shifts associated with the background and with the resonance are simply added³², so that their contributions to the Wigner scattering time delay are also additive. This results from the unitary scattering S -matrix and it differs from the situation met in the evaluation of the photoionization time delay where the coherent sum of the resonant and non-resonant components of the PDA is considered. The half Wigner time delay reported in Fig. 5b is then a sum of the term coming from the pure Breit-Wigner form plus a non-resonant term. At the energy of 9.09 eV, the maximum value of $\frac{1}{2} \tau_W$, 182 as, results from the sum of 218 as (half of the resonant contribution) and -36 as (half of the non-resonant contribution).

Consistent with the results given in Eq. (8) and (9), half of the resonant peak Wigner time delay is comparable to the computed photoionization time delay found in the resonant contribution to the PDAs, which has a peak value of 237 as displayed in Fig. 4e and reported in Fig. 5.

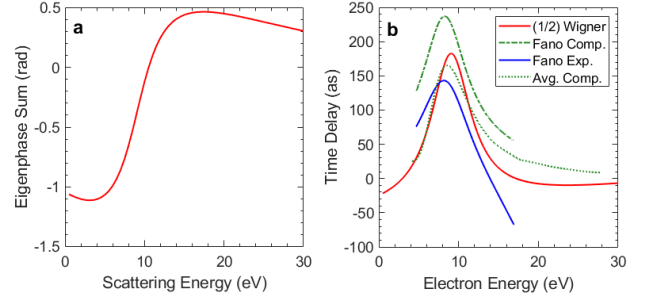


Fig. 5 Eigenphase sum and Wigner time delay for scattering from NO^+ . Eigenphase sum for e- NO^+ scattering from a one-channel calculation including only the $c^3\Pi$ state of NO^+ , with the electron-kinetic energies given relative to the threshold for that state (a). One channel $(1/2)\tau_{\text{Wigner}}$ time delay for the short-range part of the scattering phase shift compared to the photoionization time delays extracted from the resonant part of the multichannel Fano fit for theory and experiment as presented in Fig. 4e, and to the computed emission angle averaged ionization delay for the parallel orientation (see text) (b).

We note that the mean lifetime of the resonant state in the scattering resonance, using $\tau = 1/\Gamma$ (atomic units) with a width of 6.07 eV, gives a value of $\tau_w \approx 108$ as, close to the mean lifetime of the resonance extracted from the Fano model for the calculation, $\tau_{\text{res}}^T \approx 99$ as, and for the experimental data, $\tau_{\text{res}}^E \approx 83$ as. These values are also comparable to the computed emission averaged time delay for the considered parallel orientation, obtained as the average of the delay over emission directions, weighted by the differential cross sections²⁵.

This comparison shows that the resonant Wigner scattering time delay represents the main contribution to the resonant photoionization time delay at a shape resonance obtained in the multichannel Fano model. However, when considering the complete photoionization process, the non-resonant amplitudes, which combine the non-resonant scattering and the dipole coupling to the initial state, coherently add to the resonant amplitudes. This leads to the rich behavior in the angular dependence seen in the resulting PDA phases and corresponding photoionization delays.

Discussion and Conclusion

In summary, we report experimental and computed photoionization delays for one-photon ionization of the NO molecule into the $\text{NO}^+(c^3\Pi)$ state across the $4\sigma \rightarrow k\sigma^*$ shape resonance. For the selected parallel transition experiment and theory demonstrate similar variations in the range of a few hundreds of attoseconds with electron energy and emission angle in the molecular frame.

Experimental photoionization delays, completely angle-resolved in the molecular frame for fixed-in-space targets, were obtained as the energy derivative of the PDA phases, accessible through MFPADs measured at a series of photon energies using synchrotron radiation, from which the partial wave complex-valued DMEs were extracted as described, and added coherently to form the PDAs. Ab initio calculations using the multichannel Schwinger configuration interaction method with ten channels, performed at a fixed internuclear distance, compare well with those results up to the ionization delay level.

The analysis of the measured and computed complex valued PDAs based on a multichannel Fano formalism enables us to separate the photoionization dipole amplitude into resonant and non-resonant contributions. Within this model, the observed MF angle dependence of the time delay profiles results from the coherent superposition of the resonant and the non-resonant components of the PDA, where the resonance time delay is angle-independent. The in-depth description of the different contributions to the phase of the photoionization amplitude highlights the differences between the photoionization time delay and the corresponding Wigner scattering time delay.

In the future, these results could be fruitfully compared to angle-resolved two-photon ionization time delays obtained in attosecond time-resolved experiments using, e.g., the RABBITT technique combined with coincidence electron-ion 3D momentum spectroscopy. One challenging difficulty to investigate a selected photoionization process in that case resides in the congested spectra resulting from photoionization by an harmonic comb into different ionic states, even in a small molecule⁴⁶. Photoionization of NO into the $\text{NO}^+(\sigma^3\Pi)$ state stands as a favorable prototype for this goal, as illustrated by the complete MFPADs produced by an XUV attosecond pulse train which were measured for the studied process³⁴.

The time delays reported here for one-photon ionization will also provide a benchmark to disentangle the contributions from the XUV and IR transitions to the measured two-photon time-delays in a RABBITT scheme. For instance, stereo-Wigner time delays obtained in a RABBITT experiment could be compared to the here reported one-photon delays integrated over emission cones in opposite directions with respect to the orientation of the molecule.

Finally, relying on the achieved polar *and* azimuthal dependence of the PDAs and the related one-photon ionization delays when the cylindrical symmetry of the ionization process is broken, either for orientations of linear molecules other than parallel to the polarization such as the perpendicular orientation, or for non-linear polyatomic molecules where photoemission delays are foreseen as a probe of molecular environment⁴⁷, will provide additional insights into the photoionization dynamics in both spectrally and time-resolved studies, including the role of resonances in these processes.

Methods

Experimental Approach. Experiments were performed at the XUV and VUV beamlines PLEIADES and DESIRS at the Synchrotron SOLEIL operated in the 8-bunch mode (50 ps pulses with a 147 ns period)^{48,49} using circularly polarized light. MFPADs were measured using electron-ion coincidence 3D momentum spectroscopy based on a COLTRIMS-type set-up⁵⁰, taking advantage of dissociative photoionization (DPI) which results from the ejection of inner-valence shell electrons, leading to the production of an ionic fragment and a photoelectron. In this study of dissociative photoionization of NO, the velocity vectors \mathbf{v}_{N^+} and \mathbf{v}_{e} of N^+ ions and photoelectrons are derived from the impact positions

and times of flight (TOF) at the detectors, from which the MFPADs were constructed. The MFPADs are expanded using the F_{LN} -function formalism developed previously^{51,33}. DMEs were then extracted by a non-linear least-squares fit of the experimental data at each energy as described in^{51,33} giving access to the magnitudes $d_{l,m}$ and phases $\eta_{l,m}$ of the one-photon ionization dipole matrix elements. For further details on the experiments and data analysis, we refer to the Supplementary Notes 1 and 2.

Theoretical Approach. All dipole matrix elements for the photoionization of NO were computed in ten-channel calculations using the multichannel Schwinger configuration interaction (MCSCI) method described previously²⁹. These calculations were based on a close-coupling expansion of the wave function of the photoionized system including a correlated representation of a selection of the lowest lying ion states. For further details on the calculations, we refer to Supplementary Note 6.

Multichannel Fano model for a resonance. Setting $m = 0$, $\mu = 0$, and $R_{0,0}^{(1)}(\hat{\Omega} = \hat{z}) = 1$ in Eq.(2) for the studied parallel transition, the expansion of the PDA $D(\theta_k, \epsilon)$ in partial-wave DMEs $D_l(\epsilon)$ can be separated into non-resonant and resonant contributions, $D_l^{(0)}(\epsilon)$ and $D_l^{\text{res}}(\epsilon)$ (Eq. (5)) with

$$D_l^{\text{res}}(\epsilon) = \alpha_l(\epsilon) \frac{q - i}{\epsilon + i}. \quad (10)$$

In this model, the Fano line-shape parameter q is the same for all emission directions, and the quantity $\alpha_l(\epsilon)$ is related to the strength of the V_l coupling between the resonant state and each scattering partial wave l , which is assumed to be energy-independent, as follows:

$$\alpha_l(\epsilon) = V_l \left[\frac{2\pi}{\Gamma} \sum_{l'=0, \dots, l_x} D_{l'}^{(0)}(\epsilon) V_{l'}^* \right], \quad (11)$$

The total width is the sum of the partial widths Γ_l

$$\Gamma = \sum_l \Gamma_l, \quad (12)$$

where Γ_l , proportional to the rate of decay of the resonance into the l partial-wave channel, is related to the V_l coupling by

$$\Gamma_l = 2\pi |V_l|^2, \quad (13)$$

Note that the energy derivative of the phases of the $D^{\text{res}}(\theta_k, \epsilon)$ and thus the resonant time delays, as presented here, do not have any angular dependence. This is a result of the assumption that the coupling matrix elements V_l are energy independent [see Eqs. (7) and (11)].

We also note that the square of the transition matrix element if all the non-resonant D_l^0 go to zero, with $\alpha_l(\epsilon)$ also approaching zero and increasing values of q , would result in a Lorentzian function with a width of $\Gamma/2$.

In applying these formulas to the interpretation of the MFPADs in NO photoionization the non-resonant DME magnitudes $D_l^{(0)}(\epsilon)$ are assumed to be slowly varying with energy and described by a quadratic form

$$D_l^{(0)}(\epsilon) = \sum_{n=0,1,2} \epsilon^n D_{l,n}^{(0)}. \quad (14)$$

References

1. Lépine, F., Ivanov, M. Y. & Vrakking, M. J. J. Attosecond Molecular Dynamics: Fact or Fiction? *Nat. Phot.* **8**, 195–204 (2014).
2. Nisoli, M., Decleva, P., Calegari, F., Palacios, A. & Martín, F. Attosecond Electron Dynamics in Molecules. *Chem. Rev.* **117**, 10760–10825 (2017).
3. Pazourek, R., Nagele, S. & Burgdörfer, J. Attosecond Chronoscopy of Photoemission. *Rev. Mod. Phys.* **87**, 765–802 (2015).
4. Gallmann, L. *et al.* Photoemission and Photoionization Time Delays and Rates. *Struct. Dyn.* **4**, 61502 (2017).
5. Paul, P. M. *et al.* Observation of a Train of Attosecond Pulses from High Harmonic Generation. *Science* **292**, 1689 (2001).
6. Hentschel, M. *et al.* Attosecond Metrology. *Nature* **414**, 509–513 (2001).
7. Schultze, M. *et al.* Delay in Photoemission. *Science* **328**, 1658 (2010).
8. Klünder, K. *et al.* Probing Single-Photon Ionization on the Attosecond Time Scale. *Phys. Rev. Lett.* **106**, 143002 (2011).
9. Gruson, V. *et al.* Attosecond dynamics through a Fano resonance: Monitoring the birth of a photoelectron. *Science* **354**, 734 (2016).
10. Kotur, M. *et al.* Spectral phase measurement of a Fano resonance using tunable attosecond pulses. *Nat. Comm.* **7**, 10566 (2016).
11. Argenti, L. *et al.* Control of Photoemission Delay in Resonant Two-Photon Transitions. *Phys. Rev. A* **95**, 43426 (2017).
12. Heuser, S. *et al.* Angular Dependence of Photoemission Time Delay in Helium. *Phys. Rev. A* **94**, 63409 (2016).
13. Cirelli, C. *et al.* Anisotropic Photoemission Time Delays Close to a Fano Resonance. *Nat. Comm.* **9**, 955 (2018).
14. Banerjee, S., Deshmukh, P. C., Dolmatov, V. K., Manson, S. T. & Kheifets, A. S. Strong Dependence of Photoionization Time Delay on Energy and Angle in the Neighborhood of Fano Resonances. *Phys. Rev. A* **99**, 13416 (2019).
15. Busto, D. *et al.* Fano's Propensity Rule in Angle-Resolved Attosecond Pump-Probe Photoionization. *Phys. Rev. Lett.* **123**, 133201 (2019).
16. Fuchs, J. *et al.* Time Delays from One-Photon Transitions in the Continuum. *Optica* **7**, 154–161 (2020).
17. Joseph, J. *et al.* Angle-Resolved Studies of XUV–IR Two-Photon Ionization in the RABBITT Scheme. *J. Phys. B: At. Mol. Opt. Phys.* **53**, 184007 (2020).
18. You, D. *et al.* New Method for Measuring Angle-Resolved Phases in Photoemission. *Phys. Rev. X* **10**, 31070 (2020).
19. Haessler, S. *et al.* Phase-Resolved Attosecond Near-Threshold Photoionization of Molecular Nitrogen. *Phys. Rev. A* **80**, 11404 (2009).
20. Huppert, M., Jordan, I., Baykusheva, D., Conta, A. von & Wörner, H. J. Attosecond Delays in Molecular Photoionization. *Phys. Rev. Lett.* **117**, 93001 (2016).
21. Kamalov, A., Wang, A. L., Bucksbaum, P. H., Haxton, D. J. & Cryan, J. P. Electron correlation effects in attosecond photoionization of CO₂. *Phys. Rev. A* **102**, 23118 (2020).
22. Lorient, V. *et al.* High Harmonic Generation-2 ω Attosecond Stereo-Photoionization Interferometry in N₂. *J. Phys. Photonics* **2**, 24003 (2020).
23. Nandi, S. *et al.* Attosecond Timing of Electron Emission from a Molecular Shape Resonance. *Sci. Adv.* **6**, eaba7762 (2020).
24. Piancastelli, M. The Neverending Story of Shape Resonances. *J. Elec. Spectr. Rel. Phen.* **100**, 167–190 (1999).
25. Baykusheva, D. & Wörner, H. J. Theory of Attosecond Delays in Molecular Photoionization. *J. Chem. Phys.* **146**, 124306 (2017).
26. Hockett, P., Frumker, E., Villeneuve, D. M. & Corkum, P. B. Time Delay in Molecular Photoionization. *J. Phys. B: At. Mol. Opt. Phys.* **49**, 95602 (2016).
27. Vos, J. *et al.* Orientation-Dependent Stereo Wigner Time Delay and Electron Localization in a Small Molecule. *Science* **360**, 1326 (2018).
28. Cattaneo, L. *et al.* Attosecond Coupled Electron and Nuclear Dynamics in Dissociative Ionization of H₂. *Nat. Phys.* **14**, 733–738 (2018).
29. Veyrinas, K. *et al.* Dissociative Photoionization of NO Across a Shape Resonance in the XUV Range Using Circularly Polarized Synchrotron Radiation. *J. Chem. Phys.* **151**, 174305 (2019).
30. Reid, K. L. Photoelectron Angular Distributions: Developments in Applications to Isolated Molecular Systems. *Mol. Phys.* **110**, 131–147 (2012).
31. Ueda, K. *et al.* Roadmap on Photonic, Electronic and Atomic Collision Physics: I. Light–Matter Interaction. *J. Phys. B: At. Mol. Opt. Phys.* **52**, 171001 (2019).
32. Hazi, A. U. Behavior of the Eigenphase Sum Near a Resonance. *Phys. Rev. A* **19**, 920–922 (1979).
33. Lebech, M. *et al.* Complete Description of Linear Molecule Photoionization Achieved by Vector Correlations Using the Light of a Single Circular Polarization. *J. Chem. Phys.* **118**, 9653–9663 (2003).
34. Veyrinas, K. *et al.* Molecular Frame Photoemission by a Comb of Elliptical High-Order Harmonics: A Sensitive probe of both Photodynamics and Harmonic Complete Polarization State. *Faraday Discuss.* **194**, 161–183 (2016).
35. Cherepkov, N. A. *et al.* K-shell Photoionization of CO: II. Determination of Dipole Matrix Elements and Phase Differences. *J. Phys. B: At. Mol. Opt. Phys.* **33**, 4213–4236 (2000).
36. Schoun, S. B. *et al.* Precise Access to the Molecular-Frame Complex Recombination Dipole through High-Harmonic Spectroscopy. *Phys. Rev. Lett.* **118**, 33201 (2017).
37. Motoki, S. *et al.* Complete Photoionization Experiment in the Region of the $2\sigma_g \rightarrow \sigma_u$ Shape Resonance of the N₂ Molecule. *J. Phys. B: At. Mol. Opt. Phys.* **35**, 3801–3819 (2002).
38. Fano, U. Effects of Configuration Interaction on Intensities and Phase Shifts. *Phys. Rev.* **124**, 1866–1878 (1961).
39. Kabachnik, N. M. & Sazhina, I. P. Angular Distribution and Polarization of Photoelectrons in the Region of Resonances. *J. Phys. B: At. Mol. Phys.* **9**, 1681–1697 (1976).
40. Starace, A. F. Behavior of Partial Cross Sections and Branching Ratios in the Neighborhood of a Resonance. *Phys. Rev. A* **16**, 231–242 (1977).

41. Grum-Grzhimailo, A. N., Fritzsche, S., O'Keeffe, P. & Meyer, M. Universal Scaling of Resonances in Vector Correlation Photoionization Parameters. *J. Phys. B: At. Mol. Opt. Phys.* **38**, 2545–2553 (2005).
42. Lucchese, R. R. A Simple Model for Molecular Frame Photoelectron Angular Distributions. *J. Elec. Spectr. Rel. Phen.* **141**, 201–210 (2004).
43. Wigner, E. P. Lower Limit for the Energy Derivative of the Scattering Phase Shift. *Phys. Rev.* **98**, 145–147 (1955).
44. Smith, F. T. Lifetime Matrix in Collision Theory. *Phys. Rev.* **119**, 2098 (1960).
45. Taylor, J. R. *Scattering Theory. The Quantum Theory of Nonrelativistic Collisions* (Dover Publications, Mineola NY, 2006).
46. Jordan, I. & Wörner, H. J. Extracting attosecond delays from spectrally overlapping interferograms. *Journal of Optics* **20**, 24013 (2018).
47. Biswas, S. *et al.* Probing molecular environment through photoemission delays. *Nat. Phys.* **16**, 778–783 (2020).
48. PLEIADES beamline. Available at <https://www.synchrotron-soleil.fr/en/beamlines/pleiades>.
49. Nahon, L. *et al.* DESIRS: a state-of-the-art VUV beamline featuring high resolution and variable polarization for spectroscopy and dichroism at SOLEIL. *J. Synchrotron Rad.* **19**, 508–520 (2012).
50. Ullrich, J. *et al.* Recoil-Ion and Electron Momentum Spectroscopy: Reaction-Microscopes. *Rep. Prog. Phys.* **66**, 1463–1545 (2003).
51. Lucchese, R. R. *et al.* Polar and Azimuthal Dependence of the Molecular Frame Photoelectron Angular Distributions of Spatially Oriented Linear Molecules. *Phys. Rev. A* **65**, 20702 (2002).

Acknowledgements

We gratefully acknowledge J. Bozek PLEIADES-SOLEIL beamline manager, C. Nicolas and A. Milosavljevic, PLEIADES beamline scientists, E. Robert, beamline engineer assistant on PLEIADES beamline, and L. Nahon, DESIRS-SOLEIL beamline manager, G. Garcia, DESIRS beamline scientist, J. F. Gil, beamline engineer assistant on DESIRS beamline, for their cooperation and support. We thank the SOLEIL general staff for smoothly operating the facility. We are grateful to K. Veyrinas, M. Hervé and M. Gisselbrecht for their contribution to the experiment. We thank J. Guigand, S. Lupone, N. Tournier, O. Moustier (ISMO) for technical support in maintenance of the CIEL set-up. RL and DD acknowledge fruitful discussions with P. Salières. DD is very grateful for stimulating discussions with T. Jahnke within the ASPIRE ITN.

This work is supported by “Investissements d’Avenir” LabEx PALM (ANR-10-LABX-0039-PALM), EquipEx ATTOLAB (ANR-11-EQPX-0005-ATTOLAB), and ASPIRE Marie Skłodowska-Curie ITN (EU-H2020 ID: 674960). The theoretical research performed at Lawrence Berkeley National Laboratory was supported by the DOE, Office of Science, Office of Basic Energy Sciences, Chemical Sciences, Geosciences, and Biosciences Division, under Contract No. DE-AC02-05CH11231. This research used the resources of the National Energy Research Scientific Computing Center, a DOE Office of Science User Facility, and the Lawrence computational cluster resource provided by the IT Division at the Lawrence Berkeley National Laboratory.

Author Contributions

F.H., J.J., M.L., J.-C.H. and D.D. performed the measurements at the synchrotron beamlines. F.H., J.J. and J.-C.H. analyzed the experimental data. R.L. and F.H. developed and performed the fitting routines. R.L. developed the theoretical models and calculations. D.D. supervised the project. The manuscript was written by F.H., D.D., and R.L.

Supplementary Information

Influence of Shape Resonances on the Angular Dependence of Molecular Photoionization Delays

F. Holzmeier et al.

Table of Contents

Supplementary Note 1: Experimental setup.....	2
Supplementary Note 2: Extraction of experimental MFPADs	2
Supplementary Note 3: Photoionization dipole amplitudes and time delays in the molecular frame.....	3
Supplementary Note 4: Extraction of experimental DMEs from measured MFPADs	4
Supplementary Note 5: Effect of using relative phases	6
Supplementary Note 6: Calculation of the partial-wave dipole matrix elements and scattering S -matrix.	7
Supplementary Note 7: One-dimensional representation of the PDA magnitude, phase and delay	9
Supplementary Note 8: Compartments of the PDA curves in the complex plane in the Fano model ..	10
Supplementary References.....	11

Supplementary Note 1: Experimental setup

The monochromatized synchrotron radiation has a bandwidth of around 2.5 meV in the employed energy range and is focused at the center of a COLTRIMS-type 3D electron-ion coincidence momentum spectrometer. This set-up, derived from earlier versions^{1,2}, is optimized here to investigate dissociative photoionization of molecules which occurs at the intersection of the light beam and a supersonic molecular beam generated through a 70 μm nozzle and two skimmers (500 and 700 μm diameter). Ions and electrons, guided towards time and position sensitive delay line detectors (RoentDek DLD-80) by a set of variable electrostatic and magnetic fields, combined with an electrostatic lens focusing the trajectories of energetic ion fragments³, are collected over a 4π solid angle. In the study of dissociative photoionization of NO, the velocity vectors \mathbf{v}_{N^+} and \mathbf{v}_e of N^+ ions and photoelectrons are derived from the impact positions and time of flight at the detectors employing a multichannel time to digital converter for positions and ion time of flight and a synchronized time to amplitude converter for the electron time of flight³.

Supplementary Note 2: Extraction of experimental MFPADs

In this work, we investigate photoionization of $\text{NO}(X^2\Pi)$ to the $\text{NO}^+(c^3\Pi, v=0)$ state, with the ionization potential $\text{IP}=21.73$ eV corresponding to ionization from the 4σ inner valence molecular orbital, dissociating to the $\text{N}^+(^3P) + \text{O}(^3P)$ limit at 21.03 eV relative to the $\text{NO}(X^2\Pi, v=0)$ origin. In brief, the coincident events (N^+, e) corresponding to this DPI process were selected from the electron-ion kinetic-energy correlation histogram, and the MFPAD $I(\hat{k}, \hat{\Omega}) = I(\theta_k, \phi_k, \chi, \gamma)$ was constructed from the $(\mathbf{v}_{\text{N}^+}, \mathbf{v}_e)$ ion and photoelectron velocity vectors, as described in⁴ and references therein, within the axial-recoil approximation⁵. $\hat{k} \equiv (\theta_k, \phi_k)$ defines the emission direction in the molecular frame with θ_k and ϕ_k being the polar and azimuthal angles of \mathbf{v}_e relative to \mathbf{v}_{N^+} . The Euler angles $\hat{\Omega} \equiv (\gamma, \chi, \beta)$ with the polar and azimuthal angle of \mathbf{v}_{N^+} relative to the light quantization axis \hat{e} χ and γ , define the orientation of the molecular axis, i.e., the rotation of the molecular frame into the field frame (FF).

The MFPADs are expanded using the F_{LN} -function formalism developed previously^{6,7}. For dissociative photoionization of linear molecules induced by circularly polarized light, within the dipole approximation, the $I(\theta_k, \phi_k, \chi)$ MFPAD is determined by five one-dimensional $F_{LN}(\theta_k)$ functions according to the general expression⁷:

$$\begin{aligned}
 I_{\pm}(\theta_k, \phi_k, \chi) = & F_{00}(\theta_k) - \frac{1}{2}F_{20}(\theta_k)P_2^0(\cos \chi) \\
 & - \frac{1}{2}F_{21}(\theta_k)P_2^1(\cos \chi) \cos \phi_k \\
 & - \frac{1}{2}F_{22}(\theta_k)P_2^2(\cos \chi) \cos(2\phi_k) \\
 & \pm F_{11}(\theta_k)P_1^1(\cos \chi) \sin \phi_k
 \end{aligned}
 \tag{S1}$$

where P_L^N are the associated Legendre polynomials. The F_{LN} functions and their statistical uncertainties extracted from the fit of the measured $I(\theta_k, \phi_k, \chi)$ distribution according to Eq. (S1) enable us to reconstruct the MF emission diagram $I_{\chi}(\theta_k, \phi_k)$ for any orientation of the molecular axis relative to the quantization axis of circularly or linearly polarized light. In particular, for a molecular orientation parallel to the polarization of linearly polarized light considered to characterize the role of the $4\sigma \rightarrow k\sigma^*$ shape resonance, the MFPAD is fully described with

$$I_{\chi=0^\circ}(\theta_k) = F_{00}(\theta_k) + F_{20}(\theta_k).
 \tag{S2}$$

and, e.g., for a molecular perpendicular orientation it writes as

$$I_{\chi=90^\circ}(\theta_k, \phi_k) = F_{00}(\theta_k) - 0.5F_{20}(\theta_k) + 3F_{22}(\theta_k) \cos(2\phi_k). \quad (\text{S3})$$

Experimental data were recorded at eleven photon energies corresponding to the harmonics of a 800 nm Ti:Sa laser typically used in attosecond XUV+IR RABBITT-type experiments between 23.25 eV (H15) and 38.75 eV (H25), plus the 22.5 eV and 48.4 eV energies.

Supplementary Note 3: Photoionization dipole amplitudes and time delays in the molecular frame

The MFPAD $I(\hat{k}, \hat{\Omega}, E)$, i.e., the angular photoemission probability in the molecular frame (MF) for fixed-in-space molecules, is proportional to the absolute square of the photoionization amplitude $D(\hat{k}, \hat{\Omega}, E)$,

$$I(\hat{k}, \hat{\Omega}, E) = \frac{4\pi^2 h\nu}{c} |D(\hat{k}, \hat{\Omega}, E)|^2. \quad (\text{S4})$$

The photoionization amplitude can be written as

$$D(\hat{k}, \hat{\Omega}, E) = \left\langle \Psi_{\hat{k}}^{(-)}(E) \left| \vec{r} \cdot \vec{E}(\hat{\Omega}) \right| \Psi_0 \right\rangle \quad (\text{S5})$$

where $\Psi_{\hat{k}}^{(-)}$ is the wave function of the final state for the emitted photoelectron in the MF with a kinetic energy E , Ψ_0 is the initial state, \vec{r} the dipole operator, \vec{E} is the electric field. In the dipole approximation, with circularly polarized light propagating in the \hat{z}_{FF} direction and helicity $h = \pm 1$, or with light linearly polarized in the $\hat{x}_{\text{FF}} \equiv (\chi, \gamma)$ direction, for which we take $h = 0$, the corresponding PDA, can be written as

$$D(\hat{k}, \hat{\Omega}, E) = \sum_{\mu} \left\langle \Psi_{\hat{k}}^{(-)}(E) \left| r_{\mu} \right| \Psi_0 \right\rangle R_{\mu,h}^{(1)}(\hat{\Omega}). \quad (\text{S6})$$

where $R_{\mu,h}^{(1)}(\hat{\Omega})$ is a rotation matrix and $r_{\mu} = \sqrt{\frac{4\pi}{3}} r Y_{1,\mu}(\theta, \phi)$ is the dipole operator with μ being the projected angular momentum of the photon on the molecular axis. The N electron final scattering state including the $(N - 1)$ ion state and the photoelectron is currently expanded in partial waves as

$$\Psi_{\hat{k}}^{(-)}(E) = e^{-i\sigma_0} \sum_{l,m} i^l e^{-i\Delta\sigma_l} \psi_{l,m}^{(-)}(E) Y_{l,m}^*(\hat{k}) \quad (\text{S7})$$

where the σ_l are the Coulomb scattering phases, $\sigma_l = \arg \Gamma\left(l + 1 - \frac{i}{k}\right)$, and $\Delta\sigma_l = \sigma_l - \sigma_0$. Note that σ_0 is singular as $k \rightarrow 0$ and behaves as

$$\sigma_0 \rightarrow \frac{1}{k} (\ln k + 1) - \frac{\pi}{4} \quad (\text{S8})$$

where k is the photoelectron momentum $E = \left(\frac{1}{2}\right) k^2$, but the $\Delta\sigma_l$ are all finite at $k=0$. The dipole matrix element for each partial wave (DMEs) is defined as

$$\begin{aligned} D_{l,m,\mu}(E) &= e^{i\sigma_0} (-i)^l e^{i\Delta\sigma_l} \left\langle \psi_{l,m}^{(-)}(E) \left| r_{\mu} \right| \Psi_0 \right\rangle \\ &= d_{l,m,\mu} e^{i\eta_{l,m,\mu}} \end{aligned} \quad (\text{S9})$$

where $d_{l,m,\mu}$ is the real-valued magnitude of the DME and $\eta_{l,m,\mu}$ is its phase. Combining Eq. (S6-S9) leads to the expression of the PDA as given in Eq. (2) of the main paper:

$$D(\hat{k}, \hat{\Omega}, E) = \sum_{\mu} \sum_{l,m} D_{l,m,\mu}(E) Y_{l,m}(\hat{k}) R_{\mu,h}^{(1)}(\hat{\Omega}) \quad (\text{S10})$$

This provides then the one-photon ionization time delay $\tau(\hat{k}, \hat{\Omega}, E)$ as the energy derivative of its argument $\eta(\hat{k}, \hat{\Omega}, E)$:

$$\tau(\hat{k}, \hat{\Omega}, E) = \frac{d \arg(D(\hat{k}, \hat{\Omega}, E))}{dE} = \frac{d\eta(\hat{k}, \hat{\Omega}, E)}{dE} \quad (\text{S11})$$

Supplementary Note 4: Extraction of experimental DMEs from measured MFPADs

The determination of the partial-wave dipole matrix elements $D_{l,m,\mu}$ relies on the expansion of the five F_{LN} functions in Legendre polynomials:

$$F_{LN}(\theta_k) = \sum_{L'=0}^{2L_x} C_{L'LN} P_{L'}^N(\cos \theta_k), \quad (\text{S12})$$

where the $C_{L'LN}$ coefficients are expressed in terms of the DMEs as

$$C_{L'LN} = \frac{2\pi\hbar\nu}{c} \sum_{l',m',\mu'}^{l,m,\mu} (-1)^{m'+\mu'} \left[\frac{(2l+1)(2l'+1)(l'-N)!(l-N)!}{(l'+N)!(l+N)!} \right]^{\frac{1}{2}} \times D_{l,m,\mu} D_{l',m',\mu'}^* \langle ll'00|L'0\rangle \langle l',l',m',-m'|L'N\rangle \times \langle 1,1,\mu,-\mu'|L,N\rangle f_{N,L} \quad (\text{S13})$$

$$f_{N,L} = \begin{cases} \frac{1}{2} \langle 1,1,0,0|L,0\rangle & \text{if } N = 0 \\ \langle 1,1,0,0|L,0\rangle & \text{if } L = 2 \text{ and } N \neq 0 \\ i \langle 1,1,-1,1|L,0\rangle & \text{if } L = 1 \text{ and } N = 1 \end{cases}$$

Note that in the studied reaction, to a very good approximation, only $m = \mu$ DMEs contribute to the PDA, so we drop the μ label in the following.

For each photon energy, a non-linear least-squares fit of the experimental data, as described in^{6,7}, is performed giving access to the magnitudes $d_{l,m}$ and phases $\eta_{l,m}$ of the one-photon ionization dipole matrix elements. The experimental $F_{LN}(\theta_k)$ functions (Eq. (S12)) were used to generate a set of MFPAD data for a range of θ_k angles, with the light quantization axis being parallel, perpendicular, and at the magic angle with respect to the molecular axis, and with both linear and circular polarization, for a total of 113 data points that were fit at each photon energy. The parameter space of possible dipole matrix elements was sampled, usually with 10,000 random initial parameter sets, with the only constraint being that the total cross section was the same as that of the data being fit. The parameters at the nearest local minimum of the sum of the squares of the deviations, starting from each initial parameter set, were then found using the Levenberg–Marquardt algorithm. For the studied energies, a single local minimum, or two local minima corresponding to a similar quality of the fits, were found, which were significantly better than all the other fits⁷. In the presence of two solutions, the selection was based on a criterion of closest resemblance with the calculation. The statistical uncertainties of the DMEs were deduced from the root-mean-square (rms) deviation of the fit.

The MFPADs measured at different excitation energies were normalized relative to the total cross section for PI into the $\text{NO}^+(c^3\Pi)$ ionic state^{8,9}; here we chose to calibrate the measured C_{000} Legendre polynomial coefficients to those obtained in the reported calculations. On the other hand, we have used the phase of a selected partial-wave DME, here the $\eta_{2,1}$ phase of the $(d\pi)$ partial wave, which is not affected by the shape resonance (sec. III.), as a phase reference for all DMEs at the different excitation energies, such that $\tilde{\eta}_{lm} = \eta_{lm} - \eta_{2,1}$. Choosing such a common reference establishes the desired consistency between the different energies. It also removes the low energy divergence of the Coulomb phase from the phase of the PDAs. The effect of using such relative phases is discussed further in Supplementary Note 5. We note that, if desired, the part of the Coulomb phase that was subtracted with the reference phase could be reintroduced by multiplying all DMEs by $\exp(i\sigma_{l=2})$ (see Eq. (S9)).

Fig. S1 shows the experimental and computed DME magnitudes and phases as a function of the electron/photon energy. Relying on the smooth dependence of the DMEs across a broad shape resonance (see also Fig. S1 b,d for the theory), a spline fit of the experimental data was used to obtain the PDAs on a finer energy grid. To improve the fit at the boundaries of the eleven main data points, additional data points recorded at 22.5 eV and 48.4 eV were used.

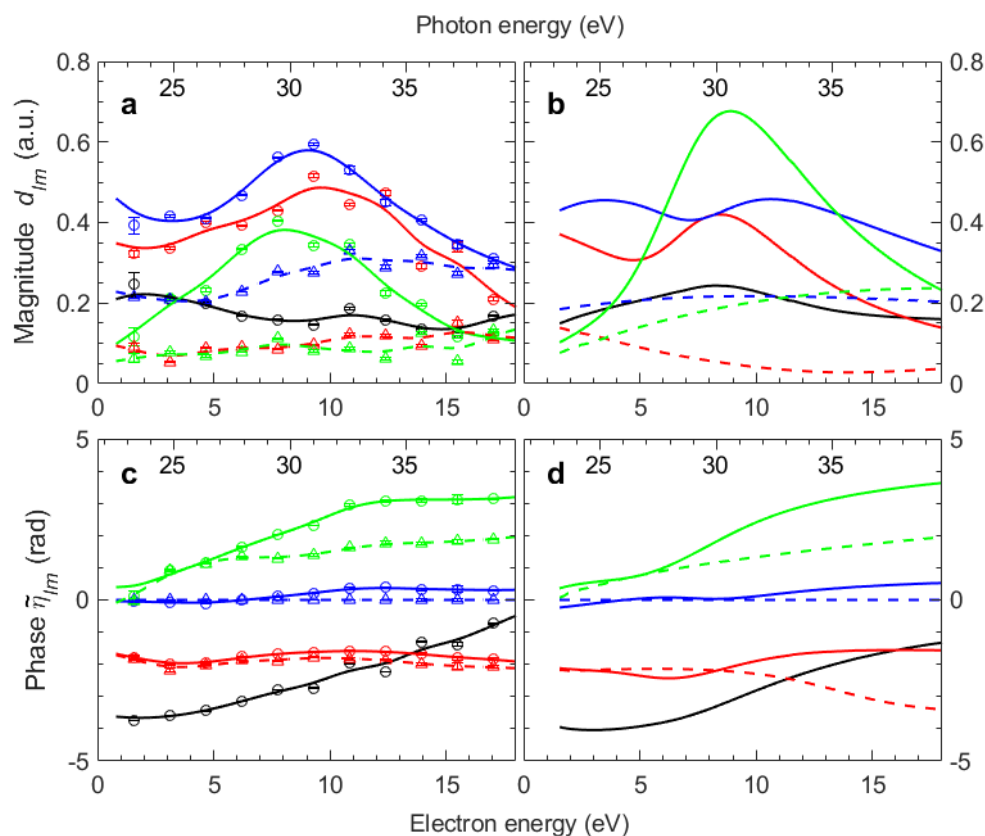


Fig. S1 Magnitudes and phases of the partial wave dipole matrix elements. **a,c** Experimental and **b,d** computed magnitudes and phases of the partial-wave DMEs as a function of the photoelectron (and photon) energy for different values of (l, m) , (black line (0,0); red line: (1,0); blue line: (2,0); green line: (3,0); red dashed line: (1,1); blue dashed line: (2,1); green dashed line: (3,1)). Error bars (two standard deviations) feature the statistical uncertainties in extracting the DME magnitudes and phases. The full and dashed lines in **a** and **c** are spline fits to the experimental data. The phases $\tilde{\eta}_{lm}$ are relative to the phase $\eta_{2,1}$.

The magnitudes of the $(l, 0) \equiv (l\sigma)$ DMEs, describing the parallel transition, dominate the explored energies, with a characteristic strong contribution of the $(f\sigma)$ partial wave from the $4\sigma \rightarrow k\sigma^*$ shape resonance clearly identified both in the measured and computed DMEs. The $(p\sigma)$ and $(d\sigma)$ partial waves are also found to take part in the resonance for the measured MFPADs. All extracted phases are referenced to the phase of the $(d\pi)$ partial wave, which is not affected by the resonance and displays a slow variation with the energy (see Fig. S2): $\tilde{\eta}_{lm} = \eta_{lm} - \eta_{21}$. The $\tilde{\eta}_{lm}$ phases do not include the low energy singularity which comes from the long-range Coulomb potential.

Supplementary Note 5: Effect of using relative phases

In Fig. S2, we give the computed absolute DME phases including the Coulomb phases for the photoionization of NO to the $c^3\Pi$ state of NO^+ . The effect of the Coulomb phase is most noticeable at low energies. The non-Coulomb phase of the $(l,m)=(2,1)$ DME, whose magnitude dominates the perpendicular transition unaffected by the σ^* shape resonance (cf. Fig. S1), displays a weak variation in the studied energy range. It is chosen as a reference for the phases of all (l,m) DMEs providing the $\tilde{\eta}_{lm} = \eta_{lm} - \eta_{21}$ phases reported in Fig. S1c and d. This subtraction removes the divergence in the Coulomb phase at low energy from the phase of each partial-wave DME.

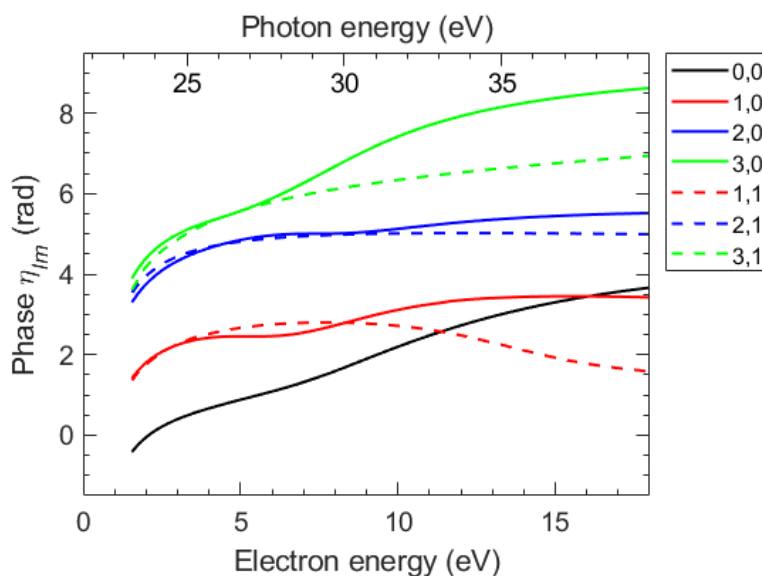


Fig. S2 Computed absolute DMEs. Variation of the computed absolute phases of the partial-wave dipole matrix elements, defined in Eq. (2), as a function of electron energy.

Fig. S3 shows a comparison of the computed absolute phases of the PDAs (a) and the corresponding time delays (c) obtained as their energy derivatives, with those obtained by summing the partial-waves DMEs referenced to the $\eta_{2,1}$ phase (b,d). One sees that in terms of photoionization time delays, adding back in the Coulomb phase results in adding a large and positive time delay (several hundreds of as) at low photoelectron kinetic energy, independent of the emission direction.

Taking such a reference thus removes the rapid rise of the Coulomb phase at low electron energies and the resulting positive contribution to the time delays, highlighting specifically the influence of the scattering from the short-range molecular potential and the dipole coupling from which the electron is removed. As stated in Note 4, the standard contribution of the Coulomb phase can be added back in analytically if desired (cf. Eq. (S9)).

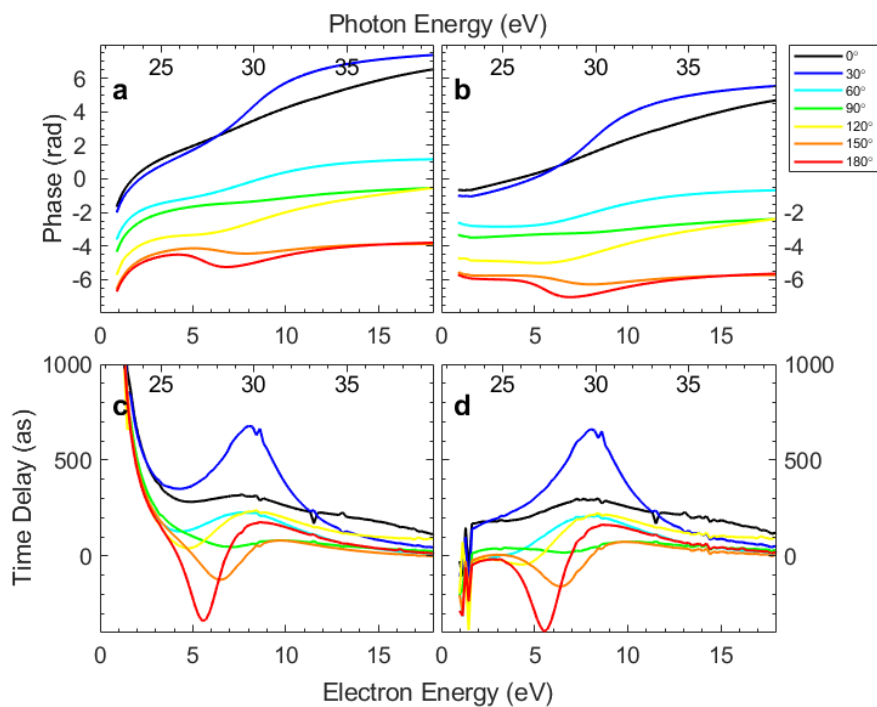


Fig. S3 Computed absolute PDA phases and ionization delays for fixed emission directions. The full absolute phases and time delays of the computed PDAs near threshold are presented for fixed emission directions in the molecular frame. **a,c** Absolute phases including Coulomb phases and corresponding ionization delays. **b,d** Computed results relative to $\eta_{2,1}$.

Supplementary Note 6: Calculation of the partial-wave dipole matrix elements and scattering S -matrix.

The DMEs reported in Fig. S1 providing the theoretical PDAs and photoionization time delays presented in Fig. 2 and Fig. S4 for photoionization of $\text{NO}(X^2\Pi)$ to the $c^3\Pi$ state of NO^+ , corresponding to ionization from the 4σ inner valence molecular orbital, were computed using the multichannel Schwinger configuration interaction method as described in ⁴. Briefly, the calculations utilized a single-center expansion, with $l_{\text{max}} = 60$, and the ion and initial states were given by complete active space configuration interaction wave functions with 8 active orbitals (four σ orbitals and four π orbitals) obtained from a valence complete active space self-consistent field calculation on the ground state of the molecule. They were performed at a fixed inter-nuclear distance of 1.15077 \AA^{10} (experimental r_e) with an augmented correlation-consistent polarized valence triple-zeta basis^{11,12} to represent the bound orbitals. The photoionization calculation^{8,13} used a close-coupling expansion of the photoionized state, including ten open channels with ion states of vertical ionization potentials near or below the ionization potential of the $c^3\Pi$ state. The states included were the $X^1\Sigma^+$, $a^3\Sigma^+$, $b^3\Pi$, $w^3\Delta$, $b'^3\Sigma^-$, $A'^1\Sigma^-$, $A^1\Pi$, $W^1\Delta$, $c^3\Pi$, and $B^1\Pi$ states. These calculations successfully describe the role of electronic correlations in photoionization of NO leading to the $c^3\Pi$ state, as well as the $4\sigma \rightarrow k\sigma^*$ shape resonance which affects the parallel component of the transition⁷.

In order to extract the resonant scattering time delay coming only from the shape resonance in the $c^3\Pi$ channel, we used a one-channel scattering calculation restricted to the $c^3\Pi$ state of NO^+ and to the σ

symmetry. The boundary conditions in the scattering calculation were for the $\psi_k^{(+)}$ scattering state (i.e. normal scattering state) which has an incoming Coulomb wave with asymptotic momentum \vec{k} and outgoing spherical scattered Coulomb waves. The number of partial waves was the same as in the photoionization calculations but the amplitudes were given by the scattering S -matrix and not by the photoionization transition amplitudes. Indeed, when using the same ten-state wave function expansion for the e -ion scattering calculation as was used in the photoionization calculation, there were contributions from a number of overlapping broad resonances coming from scattering from the different ion states included. This led to an eigenphase sum from which it was difficult to extract the time delay just from the resonance from scattering from $c^3\Pi$ state of NO^+ . The eigenphase sums from the single channel calculations as a function of scattering energy and half of the corresponding Wigner time delay are presented in Fig. 5.

Supplementary Note 7: One-dimensional representation of the PDA magnitude, phase and delay

Fig. S4 is a complementary representation of the 2D polar plot in Fig. 2 showing the magnitude, phase, and time delay along different emission directions for experiment and theory, respectively.

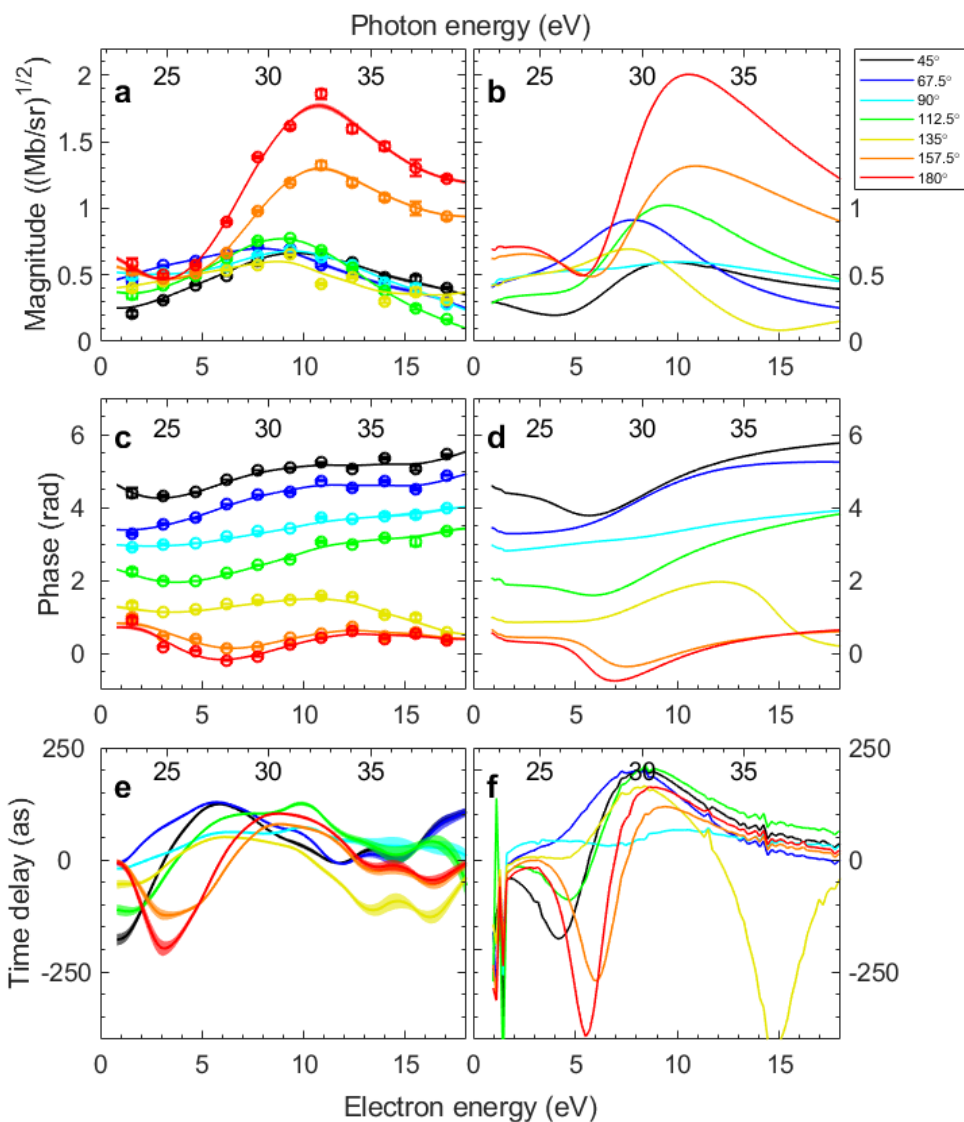


Fig. S4 Experimental and computed PDAs for selected angles. **a, c, e** Experimental and **b, d, f** computed PDAs and photoionization time delays as a function of electron (or photon) energy for selected emission angles and a molecular orientation parallel to the axis on linearly polarized light. Panels **a** and **b** represent the PDA magnitudes, panels **c** and **d** the PDA phases using the $\eta_{2,1}$ phase as a reference for the D_{lm} DME phases, and panels **e** and **f** the corresponding photoionization time delays. In (**a, c, e**) the thickness of the lines features the statistical uncertainties of the PDA magnitudes and phases, and that of the photoionization time-delays, deduced from those characterizing the magnitudes and phases of the DMEs in Fig. S1.

Supplementary Note 8: Compartments of the PDA curves in the complex plane in the Fano model

To illustrate some typical behaviors of the PDA and resulting time delays in the multichannel Fano model, we combine the expressions of the PDA summed over partial waves in Eq. (3) and that of each DME given in Eq. (5) with the additional assumption that the non-resonant DMEs, $D_l^{(0)}$, do not depend on energy. Then the behavior of the PDA is given by

$$D(\theta_k, \varepsilon) = D^{(0)}(\theta_k) + \alpha(\theta_k) \frac{q-i}{\varepsilon+i}. \quad (\text{S14})$$

With these assumptions, the curves formed by the PDAs for fixed emission angles when the energy varies across the resonance are circles centered at $D_c = D^{(0)}(\theta_k) - \left(\frac{1}{2}\right) \alpha(\theta_k)(1 + iq)$ with a radius of $R_c = \left(\frac{1}{2}\right) |\alpha(\theta_k)| \sqrt{1 + q^2}$. The sources of the phase change in the PDAs can be made clear by rewriting Eq. (S14) as

$$D(\theta_k, \varepsilon) = D^{(0)}(\theta_k) - \alpha(\theta_k) + \alpha(\theta_k)(-q \sin \Delta + \cos \Delta)e^{i\Delta} \quad (\text{S15})$$

where $\Delta = -\tan^{-1}\left(\frac{1}{\varepsilon}\right)$ is the scattering phase shift due to the short-range, non-Coulomb part of the electron-molecule interaction potential in the pure Breit-Wigner form for resonant scattering. Eq. (S15) shows that the phase change in the PDA comes from both the exponential term, $e^{i\Delta}$, and the term $(-q \sin \Delta + \cos \Delta)$ which is due to the interference between the resonant and non-resonant parts of the PDA. The exponential term by itself forms a curve that is a half-circle as ε goes from $-\infty \rightarrow +\infty$ so that its phase increases by π . Multiplying the exponential term by the interference term closes this curve to become a circle. The PDA then always starts and ends with the same phase if the infinite range of ε is considered, so that its phase will change by 0 or 2π depending on the radius of the circle and the location of its center. Examples for different parameters are displayed in Fig. S5. The circles formed by the PDAs in the complex plane are shown in Fig. S5a. The resulting time delays in panel (c) may be positive or negative, with the integral under the time delay profiles being 0 or 2π in agreement with the phase data presented in panel (b).

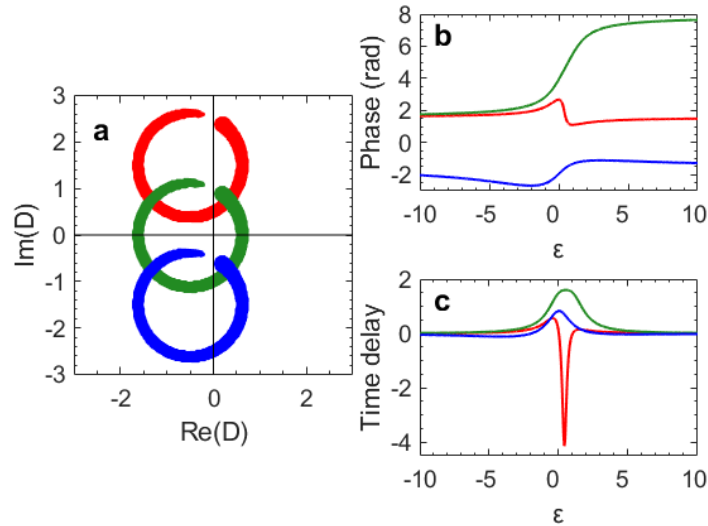


Fig. S5 Range of the behavior of PDA curves near a resonance. **a** Curves of the PDA for the model given in eq. (S14), for $q = 2.0$, $\alpha = 1.0$ and with the value of D^0 of $2.5i$ (red), $1.0i$ (green), and $-0.5i$ (blue), respectively. The increasing size of the markers indicates increasing value of the relative energy

ϵ . **b** The value of the phase of the PDA with the same set of D^0 values. **c** The energy derivative of the phases expressed as time delays. Note that in this example, since the energies are unitless quantities, the corresponding time delays are also unitless.

For the studied shape resonance in photoionization of NO, with $E_{\text{res}} \approx 8.5$ eV and $\Gamma \approx 7$ eV, the range of energies considered here is limited to about two times the width of the resonance. This leads to PDA phase changes ranging from 0 to 2π . The major photoemission process around ($\theta_k = 180^\circ$) is a clear illustration of the model, with a time delay displaying both positive and negative values, as reported in Fig. 2c and Fig. S4e and f, and a net PDA phase change close to zero. The phase change in the PDA for 60° is closer to π . This behavior results from the nearly zero non-resonant PDA at 60° , as shown in Fig. 4b. The peak in the computed photoionization time delay at 60° (202 as), seen in Fig. 2c and Fig. S4f, is also very close to the time delay of the resonant PDA (237 as) reported in Fig. 4e.

Supplementary References

1. Gisselbrecht, M., Huetz, A., Lavollée, M., Reddish, T. J. & Seccombe, D. P. Optimization of Momentum Imaging Systems Using Electric and Magnetic Fields. *Rev. Sci. Instrum.* **76**, 13105 (2004).
2. Picard, Y. J. *et al.* Attosecond Evolution of Energy- and Angle-Resolved Photoemission Spectra in Two-Color (XUV + IR) Ionization of Rare Gases. *Phys. Rev. A* **89**, 31401 (2014).
3. Lebech, M., Houver, J. C. & Doweck, D. Ion–Electron Velocity Vector Correlations in Dissociative Photoionization of Simple Molecules Using Electrostatic Lenses. *Rev. Sci. Instrum.* **73**, 1866–1874 (2002).
4. Veyrinas, K. *et al.* Dissociative Photoionization of NO Across a Shape Resonance in the XUV Range Using Circularly Polarized Synchrotron Radiation. *J. Chem. Phys.* **151**, 174305 (2019).
5. Zare, R. N. Photoejection Dynamics. *Mol. Photochem.* **4**, 1–37 (1972).
6. Lucchese, R. R. *et al.* Polar and Azimuthal Dependence of the Molecular Frame Photoelectron Angular Distributions of Spatially Oriented Linear Molecules. *Phys. Rev. A* **65**, 20702 (2002).
7. Lebech, M. *et al.* Complete Description of Linear Molecule Photoionization Achieved by Vector Correlations Using the Light of a Single Circular Polarization. *J. Chem. Phys.* **118**, 9653–9663 (2003).
8. Stratmann, R. E., Zurales, R. W. & Lucchese, R. R. Multiplet-Specific Multichannel Electron-Correlation Effects in the Photoionization of NO. *J. Chem. Phys.* **104**, 8989–9000 (1996).
9. Wallace, S., Dill, D. & Dehmer, J. L. Shape Resonant Features in the Photoionization Spectra of NO. *J. Chem. Phys.* **76**, 1217–1222 (1982).
10. Huber, K. & Herzberg, G. *Molecular Spectra and Molecular Structure. IV. Constants of Diatomic Molecules* (Springer US, New York, 1979).
11. Dunning, T. H. Gaussian basis Sets for Use in Correlated Molecular Calculations. I. The Atoms Boron Through Neon and Hydrogen. *J. Chem. Phys.* **90**, 1007–1023 (1989).
12. Kendall, R. A., Dunning, T. H. & Harrison, R. J. Electron Affinities of the First-Row Atoms Revisited. Systematic Basis Sets and Wave Functions. *J. Chem. Phys.* **96**, 6796–6806 (1992).
13. Stratmann, R. E. & Lucchese, R. R. A Graphical Unitary Group Approach to Study Multiplet Specific Multichannel Electron Correlation Effects in the Photoionization of O₂. *J. Chem. Phys.* **102**, 8493–8505 (1995).